Available online at www.sciencedirect.com

jmr&t Journal of Materials Research and Technology

journal homepage: www.elsevier.com/locate/jmrt

Original Article

Effects of heat input on metallurgical behavior in HAZ of multi-pass and multi-layer welded IN-939 superalloy

Amirhossein Mashhuriazar [a], *C. Hakan Gur* [b], *Zainuddin Sajuri* [c], *Hamid Omidvar* [a,*]

[a] *Department of Materials and Metallurgical Engineering, Amirkabir University of Technology, Tehran, 1599637111, Iran*

[b] *Department of Metallurgical and Materials Engineering, Middle East Technical University, Ankara, 06800, Turkey*

[c] *Department of Mechanical and Manufacturing Engineering, Faculty of Engineering and Built Environment, Universiti Kebangsaan Malaysia, 43600, Bangi, Selangor, Malaysia*

ARTICLE INFO

Article history:
Received 12 July 2021
Accepted 24 August 2021
Available online 3 September 2021

Keywords:
Welding
Nickel-based superalloy
IN-939
Heat treatment
Crack
Heat input

ABSTRACT

The hot components of a gas turbine are susceptible to damage in the high-temperature environment of turbine engine operation. Given that these components are relatively costly to manufacture, they are often repaired than replaced when damaged. Fusion welding is an economical method for repairing the damaged components of a gas turbine. This research examines the roles of heat input, pass number and layer number on the intergranular liquation cracking of the Inconel-939 (IN-939) precipitate nickel base superalloy during tungsten arc welding. Several specimens were welded with IN-625 filler alloy under argon gas by following the Taguchi method and an L8 array. These specimens were then characterized via metallographic investigations and hardness measurements. Results show that, during welding, the IN-939 heat-affected zone (HAZ) is acutely prone to cracks that propagate along the grain boundaries. Moreover, layer number, heat input and pass number significantly influence the microstructure and liquation cracking of HAZs with impact percentages of 72.37%, 22.17% and 4.84%, respectively.

1. Introduction

Superalloys exhibit excellent mechanical properties and high corrosion and oxidation resistance under extreme stress conditions and even near melting temperature [1]. Nickel-based superalloys exhibit significant creep resistance and strength at temperatures above 650 °C [2]. Therefore, these alloys are critical in constructing the highly elevated sections of power plants and in the aerospace industry [3–6]. Inconel-939 (IN-939) is a precipitation-hardenable (PH) nickel-based superalloy used in manufacturing hot components and

* Corresponding author.
E-mail address: omidvar@aut.ac.ir (H. Omidvar).

https://doi.org/10.1016/j.jmrt.2021.08.113

blades [7] operating at temperatures up to 850 °C under high-stress conditions [8]. Given their harsh operating conditions, these components are easily damaged through several mechanisms, including surface erosion [9], hot corrosion [10], high-temperature fatigue [11] and oxidation [12]. Although several methods for joining different types of materials are available, the damaged components are usually repaired by using industrial approaches, such as fusion welding, vacuum brazing, and diffusion bonding, given their high manufacturing costs [13–17]. In this case, the susceptibility of PH nickel-based superalloys to cracking is mainly attributed to the emergence of heat-affected zones (HAZ) during the welding process [18]. Meanwhile, the poor weldability of these superalloys may be attributed to their microstructure, which comprises a high volume fraction of gamma prime precipitation that accounts for their main strengthening phase [19].

Many studies have attempted to address the susceptibility of HAZs to cracking, with most of them focusing on the preventive effect of certain factors, such as the choice of filler metal [20], heat input [21], welding speed [22] and heat treatment before and after welding [18]. Ye et al. [23] reported a lower welding heat input combined with a pre-welding homogenization heat treatment to control and decrease liquation cracking sensitivity in multi-pass or multi-layer welding. It is because, as the welding heat input increased the weld metal columnar dendrite arm spacing and welding stress increased which, leading to an increase in weld metal solidification cracking sensitivity.

To understand the effect of filler metal composition on the weldability of IN-939, Hassan Kazempour-Liasi et al. [24] compared the liquation cracking generation in the HAZ of IN-939 weldments during TIG welding with solid solution and age-hard enable filler metals. They found that, compared with age-hard enable filler metals, the extent of liquation cracking in the HAZ is more significant when the solid solution alloy is used as a filler alloy. Ola et al. [20] reported that the HAZ intergranular liquation cracking in weldments depends on the filler alloy compound utilized during welding. Soft weld metals with a low gamma-prime volume fraction and Al+Ti+Nb+Ta concentration were perceived to be less prone to cracking than those with high Al+Ti+Nb+Ta concentration.

Researchers have studied the effect of heat treatment on microstructural response and liquation cracking of IN-939. González et al. [25] found that pre-weld heat treatment (PWHT) can influence the lattice parameters and define the extent of mismatch in the crystalline lattices of gamma-prime precipitates, structure with the low mismatch between gamma prime precipitates and substrate reduce crack formation. In their other work, González et al. [26] found that the hardness of the material before welding can affect the ability of the base metal (BM) to relax the welding stresses generated in the HAZ during cooling. They revealed that an alloy with low hardness can effectively relax HAZ stresses and lead to uncracked grain boundaries. Kazempour-Liasi et al. [27] studied the effects of PWHT cycles on the mechanical and microstructure characteristics of IN-939 alloy weldments and concluded that the cooling rate during PWHT can influence the microstructure. According to their results, applying solution annealing and swiftly cooling the microstructure of the IN939 contain coarse MC primary carbide without any gamma prime phase.

Ye et al. [21] investigated the role of welding heat input in curbing hot cracking in IN-718 sheets during tungsten inert gas (TIG) welding and found that a lower welding heat input (0.24–0.48 kJ/mm) can subside the vulnerability of these sheets to hot cracking. Chen et al. [28] tested the significance of heat input in the HAZ liquation cracking during the laser additive manufacturing of IN-718 and found that vulnerability to liquation cracking increases along with heat input. They attributed such phenomenon to thermal stress, welding process instability and interdendritic element segregation in the deposition. Mashhuriazar et al. [19] examined the effect of welding parameters on the liquation cracking behavior of IN-

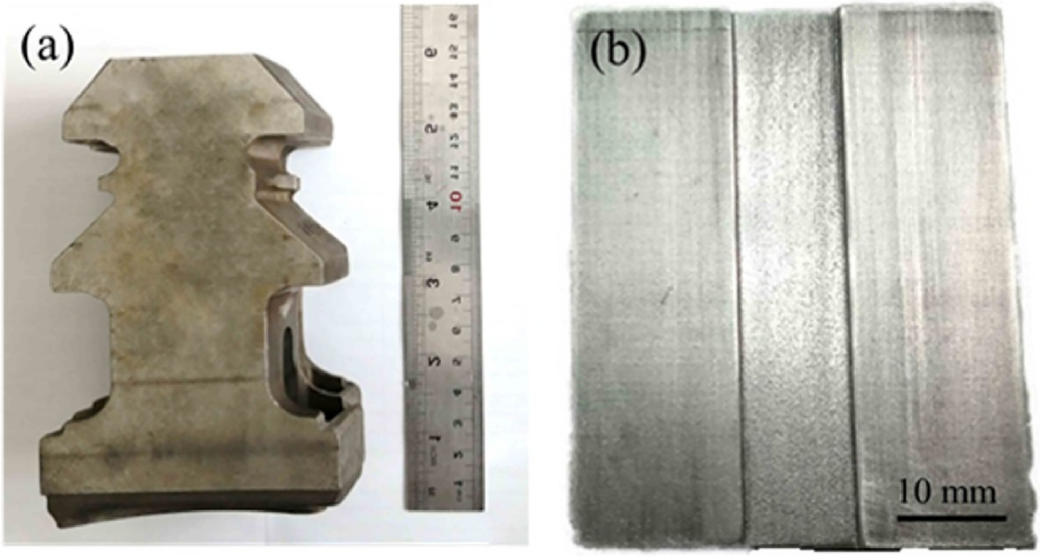

Fig. 1 – (a) Root of the gas turbine blade made of IN-939, (b) substrate of IN-939 before the welding.

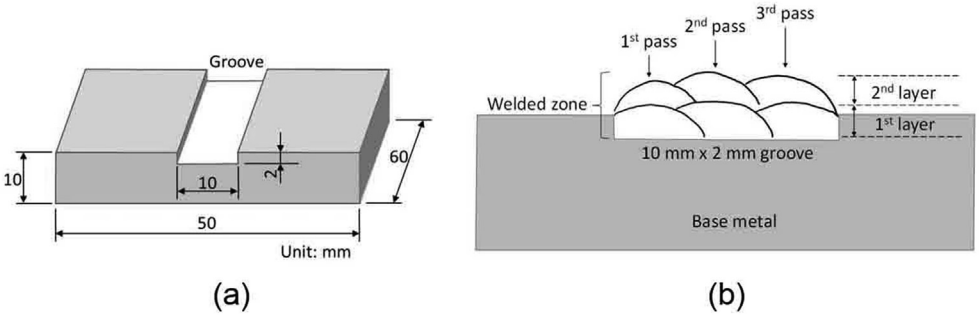

Fig. 2 – (a) Sample dimension and (b) the schematic diagram of welding procedures.

939 superalloys and found that welding parameters, such as flexural load, welding speed and heat input, significantly influence tensile stresses, the IN-939 microstructure and cracking during welding [19]. Meanwhile, using a highly ductile filler alloy and setting a low flexural load, welding speed and heat input can significantly reduce the amount of liquation cracking during fusion-repair processes [30].

It is seen here that fusion welding is the main industrial approach to repair damaged components of gas turbine engines. According to Álvarez Tejedor et al. [29], the cracked area must be cleaned, degreased and gouged or machined away sufficiently to permit a full penetration weld repair to be made, with no traces of crack left behind and no new significant defects introduced.

In this study, proper welding parameters are detailed out to evaluate the effects of heat input, layer number and number of welding passes on the microstructure and liquation cracking behavior of IN-939. To avoid the influence of any inherent defect from the base metal, only defect-free material from the root of turbine blade was used. The novelty of this study lies on the assessment of the effects of multi-pass and multi-layer repair welding on the metallurgical properties of IN-939 despite the great application significance of TIG welding. The selected specimens were evaluated through metallographic investigations and hardness measurements. Taguchi method was applied to test the effects of each parameter. The success of this work can lead to the development of a standard repair method that can be used in various industries.

2. Experimental

2.1. Materials and samples preparation

In this study, samples were prepared from the root of scrapped gas turbine (Siemens Energy, Munich, Germany) blades made of IN-939 that has been withdrawn from service as shown in Fig. 1(a). The microstructure of the root of the blade was first examined to confirm that there is no abnormality in the component and ensure that the quality of the material is not degraded. This defect-free material was then used as the sample to fulfill the objective of this study to identify the effects of welding heat input on metallurgical behavior in HAZ of multi-pass and multi-layer of IN-939 superalloy (see Fig. 2).

The welding test coupon dimensions of 60 mm × 50 mm × 10 mm with a 10 mm × 2 mm groove in the middle were prepared from the root of a turbine blade as shown in Fig. 1(b). A quality inspection on the test coupons used was performed using the radiographic examination procedure to evaluate the quality of the products and ensure that the material used for the study have no initial defects. All samples have gone through pre-welding heat treatment before proceeding to the welding test. The solution heat treatment was performed in a vacuum furnace with 10^{-5} Torr pressure (1160 °C with a dwell time of 4 h before cooling in the furnace at 2 °C/min) [30]. The chemical composition of the BM and filler metal (IN-625) are given in Table 1.

2.2. Experimental methodology

The design parameters used in the experiments are listed in Table 2. These parameters include the effect of heat input at two levels (0.45 and 0.6), number of welding pass at two levels (3 and 4) and layer number at two levels (single layer welding and multi-layer welding). The two levels of heat input were

Table 2 – Parameter design control factors and levels in the Taguchi method.

Factors	Level 1	Level 2
Heat input (kJ/mm)	0.45	0.60
Pass number	3	4
Layer number	1	2

Table 1 – Chemical composition of the base and filler metals (wt.%).

Material grade	Al	Ti	Mn	Nb	Mo	Ta	C	W	Co	Cr	Ni
IN 939	1.59	3.22	0.02	0.65	0.20	2.00	0.14	2.53	16.08	27.1	Balance
IN 625	0.40	0.40	0.50	3.15	10.00	–	1.00	–	1.00	20.00	Balance

Table 3 – Conditions and order of the welding.

Experimental samples	Heat input (kJ/mm)	Number of passes	Number of layers
S-45-3-1	0.45	3	1
S-45-3-2	0.45	3	2
S-45-4-1	0.45	4	1
S-45-4-2	0.45	4	2
S-60-3-1	0.60	3	1
S-60-3-2	0.60	3	2
S-60-4-1	0.60	4	1
S-60-4-2	0.60	4	2

decided based on the heat input range used by Ye et al. (0.24–0.48 kJ/mm) and Mashhuriazar et al. (0.45 and 0.6 kJ/mm) [20,31]. The heat input energy of the arc welding was computed as:

$$\text{Heat input} = (V \times A \times 60) / (S \times 1000) kJ / mm \quad (1)$$

where V, A and S represent the arc voltage, welding current and welding speed, respectively [30]. TIG welding with IN-625 filler was performed under argon atmosphere [31]. The TIG welding was performed at 10 V and 75 mm/min linear speed at two different welding currents of 56 and 75 A [19,30].

Multi-pass and multi-layer welding was performed with several heat inputs and based on the Taguchi method with an L8 array to determine optimum welding parameter and influence of each parameter on HAZ cracking (Table 3). The Taguchi method was used, as it decreases experimental study costs and provides a systematic approach. Also, to determine the degree of effect of each parameter, variance analysis (ANOVA) was applied. This analysis was performed at 5% significance level and 95% confidence level.

2.3. *Microstructural examination*

The micro-fissuring vulnerability of HAZ relies on the microstructure and composition of the material. Therefore, the specimens were initially ground using emery papers with grades up to 2000 before they were polished and etched with a marble solution for 7 s to reveal the microstructure at the BM and welding zone. The JMatPro V7 software was used to simulate the phase changes resulting from the applied heat inputs. An optical microscope and a field emission scanning electron microscope (FE-SEM MIRA3 XMU TESCAN) were then used to investigate the microstructure and phases of the welding zone. An EDS analysis was performed to identify the chemical composition of the joints in various areas. The microhardness of the joint specimens was measured by using a Vickers hardness tester according to ASTM E92 (with an applied force of 9.8 N and a dwell time of 15 s). ImageJ 1.44 software was used to measure the average size of various joint

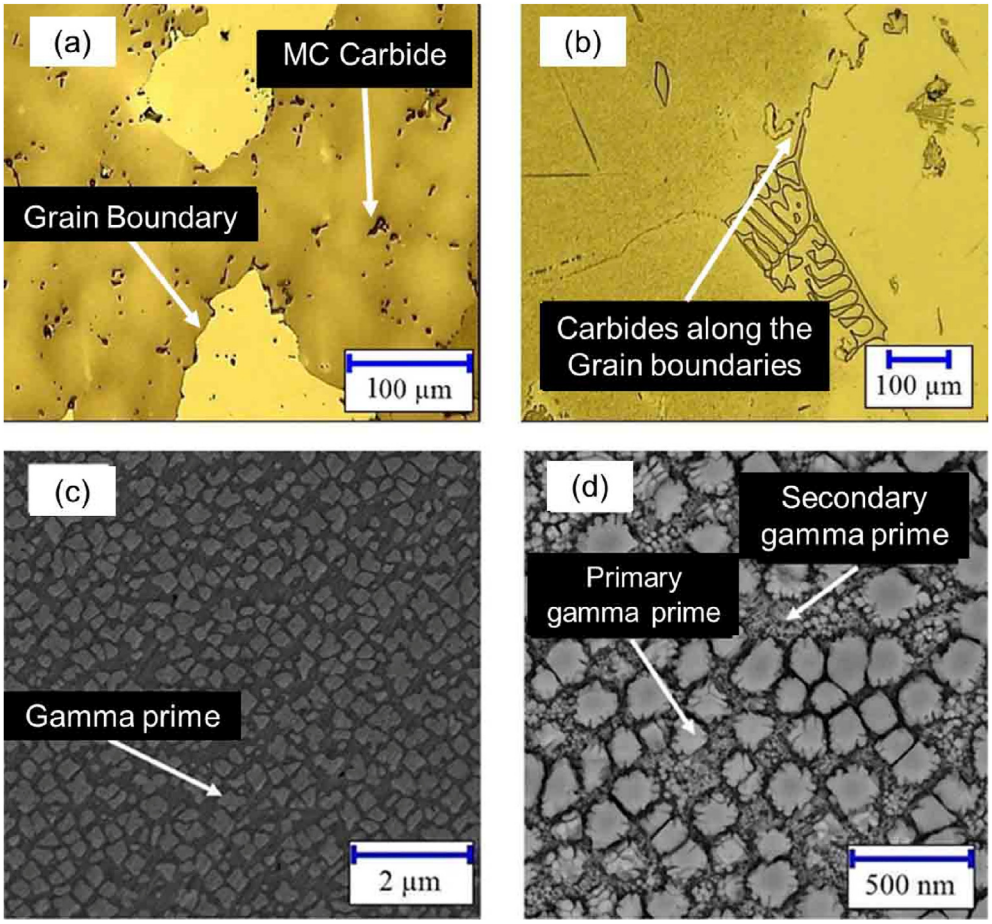

Fig. 3 – Cross-sectional view of the IN-939 base material. (a) and (b) Optical images of the MC carbide precipitated in the grain and along the grain boundary; (c) and (d) FE-SEM images of the primary and secondary gamma-prime precipitates.

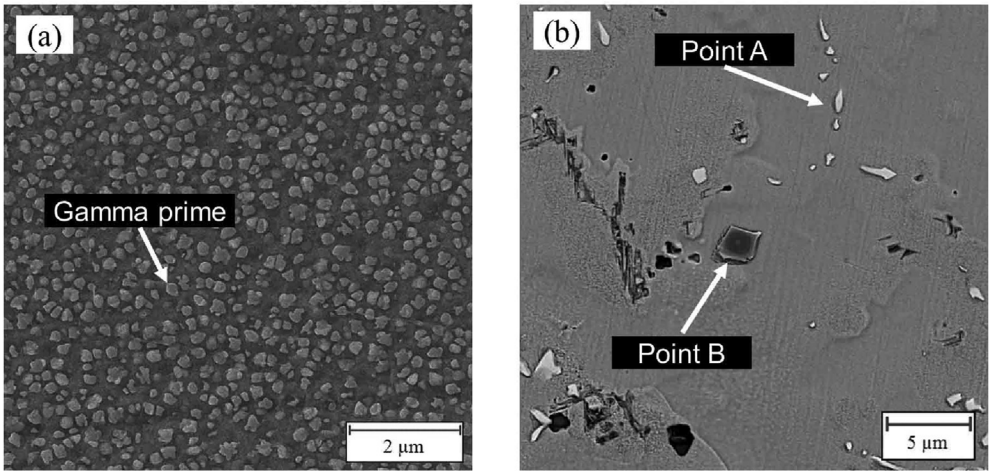

Fig. 4 – Cross-section view of the welded specimen; (a) FE-SEM images of the gamma-prime after the solution heat treatment; and (b) FE-SEM images of the carbide and eta phases in the cross-section of IN-939.

areas, number of cracks, total crack length (TCL) and average crack length (ACL) at the weld from four cross-sections. These values were then coded by using the Taguchi's method to optimize the welding process.

3. Results and discussion

3.1. *Microstructure of the service-exposed IN939*

The typical microstructure of the service-exposed IN-939 alloy comprised primary and secondary γ' particles, primary MC and $M_{23}C_6$ carbides, as shown in Fig. 3(a)–(d). The microstructure and mechanical characteristics of this superalloy changed due to harsh service exposure. Such exposure also led to the emergence of continuous grain boundary carbides and the transformation (degeneration) of MC carbides grain boundaries. This microstructural alteration during service may account for the limited ductility in the room and the high-temperature properties of the alloy. According to Abedini et al. [32], during a high-elevated service, the MC carbides within the grain boundaries can react with the γ phase (i.e., the matrix) and form new phases of η and $M_{23}C_6$ carbides. The MC carbides located in the grains did not deteriorate. This degeneration reaction of grain boundary MC carbides at temperatures below 800 °C can be formulated as [33]:

$$MC + \gamma/\gamma' \rightarrow M_{23}C_6 + \eta \quad (2)$$

Above 850 °C, the MC carbides reacted with matrix γ to generate gamma-prime and $M_{23}C_6$ carbides. Only at the large-angle grain boundaries with high interfacial energy, these $M_{23}C_6$ carbides emerged. In light of the coherent orientation correlation between $M_{23}C_6$ and the matrix, the carbides can be precipitated with four distinctive morphologies that significantly affect their mechanical characteristics [34].

3.2. *Microstructure of the heat-treated alloy*

The specimens were exposed to 1160 °C with a dwell time of 4 h before they were cooled in the furnace at 2 °C/min. Following Kazempour-Liasi et al. [35], the primary gamma-prime particle (the participant with the most critical affection on the superalloy properties) was precipitated at temperatures below 1160 °C when the cooling rate was adequately low. High cooling rates are responsible for precluding gamma-prime particles from their nucleation and growth and lead to

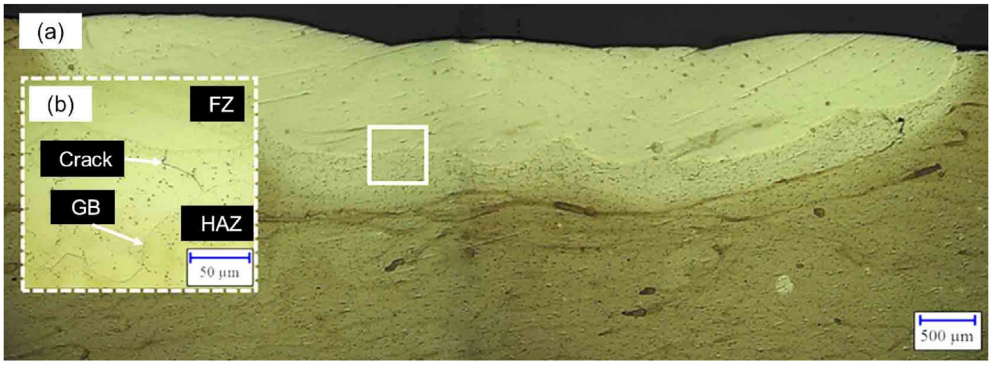

Fig. 5 – Welded sample of S-45-3-1 (0.45 kJ/mm, single layer in 3 passes): (a) Cross-section view; (b) high magnification of the crack in the weld zone.

the emergence of coarse MC primary carbide particles. Fig. 4(a),(b) present the microstructure of BM exposed to the solution heat treatment. Following the heat treatment, all gamma-prime carbides, except for the MC carbide, and η phases precipitated into the solution. After homogenization, the microstructure comprised a gamma-prime phase with an irregular morphology (particle sizes of 220 nm and 32% volume fraction), primary MC carbides and η phases. In the elemental analysis, point A obtained approximately 85 at.% of Ti and Ni, thereby suggesting the presence of the η phase, whereas point B contained C, Ti and Nb, thereby indicating the presence of MC carbide.

Carbides affect mechanical characteristics based on their morphology and distribution. During solidification, Ti-rich MC carbides in fine blocks were dispersed all over the matrix and formed separate particles in intergranular and intragranular positions among the dendrites. These carbides emerged in the liquid phase owing to a distinguished carbon separation and often reacted with Ti and Mo. Although these carbides seemed stable at low temperatures, they tend to deteriorate into secondary carbides at higher temperatures. The precipitation of thin films of $M_{23}C_6$ Cr-rich carbides at the grain boundaries can be formulated as:

$$MC + \gamma \rightarrow M_{23}C_6 + \gamma'(Ti,\ Mo)C + (Ni,\ Cr,\ Al,\ Ti) \rightarrow Cr_{21}Mo_2C_6 + Ni_3(Al,\ Ti) \quad (3)$$

3.3. Weld metal microstructure

The microstructures of the precipitation-hardened superalloy IN-939 are highly vulnerable to cracking during welding. Fig. 5 shows the microstructure of the welded sample of IN-939 and the formation of a crack in its HAZ. All cracks appeared in the HAZ and grew perpendicular to the melting zone of the grain boundaries.

Some instances of cracking in the HAZ of the pre-weld heat-treated samples are shown in Fig. 6. Intergranular cracking was reported near the secondary phases and primary carbides. The expansion of the melting area around the weld zone and the diffusion of a liquid phase in the grain boundaries and layer–matrix interface triggered the propagation of cracks in the affected area [19,30]. During the non-equilibrium heating process of multi-pass or multi-layer welding, an abundant amount of solute atoms was released from the particles and formed a diffusion area with a high composition gradient [36]. Therefore, the chemical composition between the particles and matrix can reach a point where a eutectic reaction occurs and the volume of molten material increases. Therefore, the phase distribution in terms of temperature and transformation must be explored to understand the crack initiation. To this end, the chemical composition at the weld pool and HAZ interface must be calculated along with the dilution levels (D).

Yan et al. [37] argued that the grain boundary liquation during the welding of GH909 alloy is responsible for the HAZ

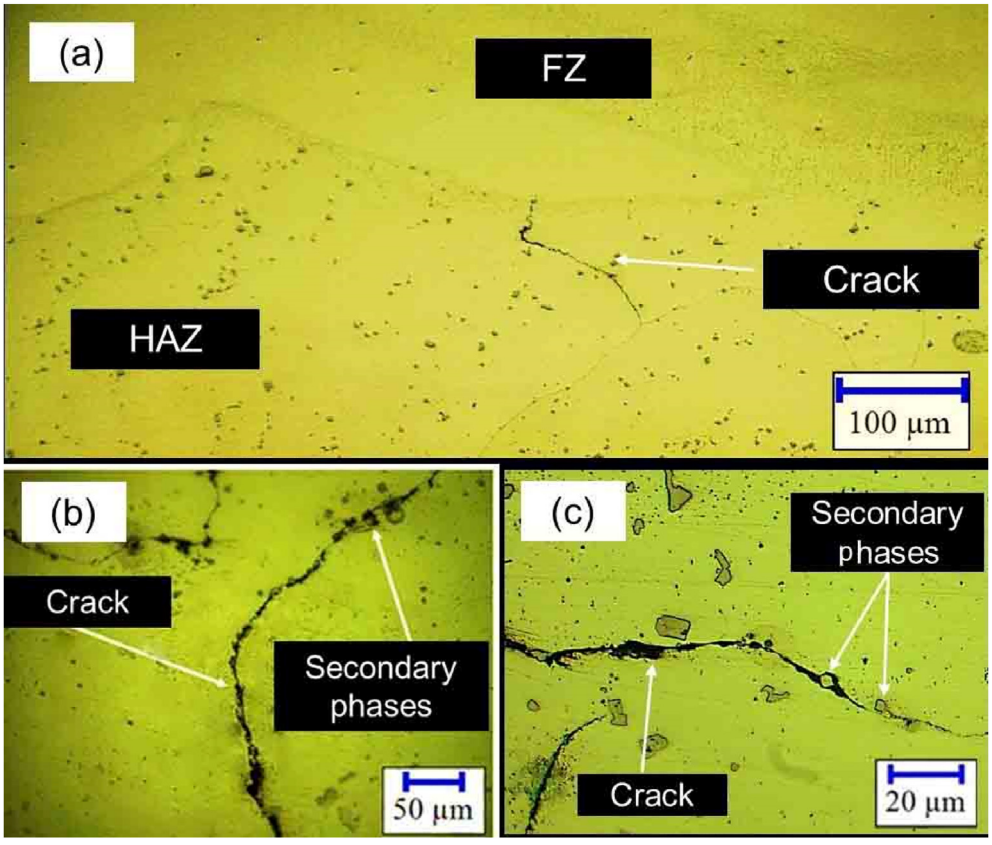

Fig. 6 – Microstructure of the welded sample of S-60-3-1 (0.6 kJ/mm, single layer in 3 passes): (a) cross-section view; (b) liquation cracks in HAZ; (c) secondary phases along the cracks.

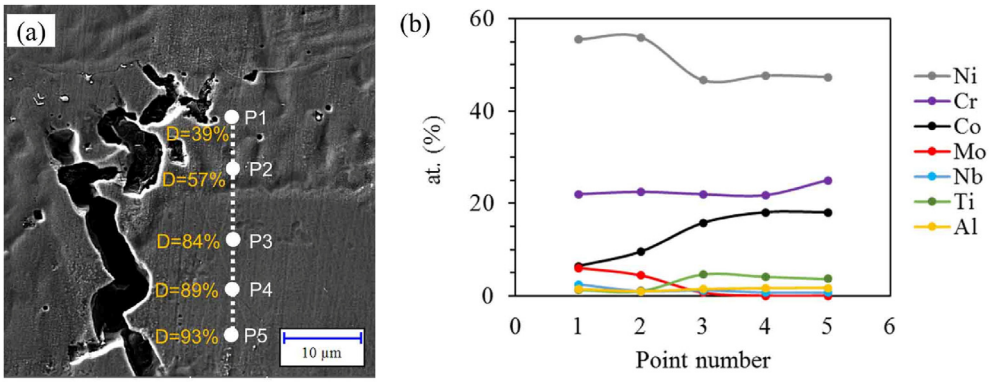

Fig. 7 – HAZ microstructure of the welded sample of S-60-3-1 (with 0.6 kJ/mm, single layer in 3 passes): (a) FE-SEM images of a crack in the HAZ, (b) EDS point analysis performed around the crack at the interface of the weld pool and HAZ.

liquation cracking. In their assessment of HAZ liquated cracking in a welded specimen, they found that cracking is associated with composition segregation. Fig. 7(a) shows the microstructure at different points surrounding a crack that emerged in the HAZs of IN-939. These grain boundary cracks were nucleated from the boundary separating the fusion zone from the HAZ and mainly propagated toward the BM. Abundant re-melting areas were found in the proximity of these cracks. MC and secondary carbides that were formed during solidification can melt in the HAZ due to the reaction between the dissolution precipitation and the matrix [38]. Under sufficient heat stress, cracks may appear along the boundaries of the HAZ region and grow in the integration area. Therefore, the potential effect of this phase on the cracking and the changes in the chemical composition of joints should be investigated.

An EDS point analysis was performed on different points to check for variations in chemical composition at the weld pool and the HAZ interface as shown in Fig. 7(b). The dilution levels (D) for each point was calculated as (Fig. 7(a)) [39]:

$$D = \frac{C_w - C_{fw}}{C_b - C_{fw}} \quad (4)$$

where D is the dilution level, C_w, C_{fw} and C_b are the elemental compositions of the fusion zone, filler metal and substrate, respectively. Table 4 compares the chemical compositions of different points at the weld zone as obtained from EDS point analysis and calculated using the JMatPro software. Table 1 presents the chemical compositions of BM and filler metal for calculations using the JMatPro software. The composition segregation and phases that exit each point were then simulated based on these results.

Fig. 8 shows the phase simulation results for IN-939 in the solidification temperature range. The solidification of IN-939 began at 1324 °C with the gamma phase nucleation. At 1314 °C, the primary MC carbide was nucleated. The solidification ended with 98.88% gamma phase and 1.12% MC carbide at 1257 °C.

The solidification of the IN-625 filler metal began at 1335 °C with the M6C carbide nucleation, followed by the $M_{23}C_6$ carbide nucleation at 1328 °C and the gamma phase nucleation at 1307 °C. The solidification ended with 81.95% gamma phase, 9.75% $M_{23}C_6$, 6.13% M_6C and 2.16% MC carbide at 1289 °C. The distribution of the solute in the solidification step was formulated as [40]:

$$C_s = KC_0[1 - fs]^{k-1} \quad (5)$$

where C_S, C_0, f_S and K denote the solid composition in the solid–liquid interface, nominal composition, solid fraction and equilibrium separation factor, respectively. The equilibrium separation factor determines the segregation of alloying elements into liquid and solid phases during solidification. K was computed at any temperature by using Equation (6), where C_S and C_L denote solid and liquid composition at a certain temperature, respectively [41]:

The K values for both IN-939 and IN-625 at different chemical compositions are shown in Table 5. These values were computed using the JMatPro software at the start (TS) and end (TL) of the solidification process. If $K < 1$, then the

Table 4 – Chemical composition of different points at the weld zone obtained via EDS point analysis and calculated using the JMatPro software.

Point No.	Chemical composition (at.%)															
	JMatPro								EDS							
	Ni	Cr	Co	C	Mo	Nb	Ti	Al	Ni	Cr	Co	C	Mo	Nb	Ti	Al
1	56.4	22.7	8.0	0.6	6.1	2.3	1.6	0.9	55.4	22.0	6.4	0.9	6.1	2.5	1.4	1.5
2	53.1	23.8	10.9	0.5	4.6	1.9	2.1	1.2	55.9	22.5	9.5	0.8	4.5	1.0	1.1	1.0
3	46.6	26.0	16.4	0.3	1.5	1.3	3.2	1.6	46.6	22.0	15.7	0.8	0.8	1.2	4.7	1.5
4	45.8	26.3	17.2	0.3	1.1	1.2	3.7	1.7	47.6	21.8	18.0	0.8	0.1	0.7	4.2	1.7
5	46.2	26.1	17.7	0.2	0.8	1.1	3.4	1.7	47.3	25.0	18.0	0.9	0.1	0.7	3.7	1.8

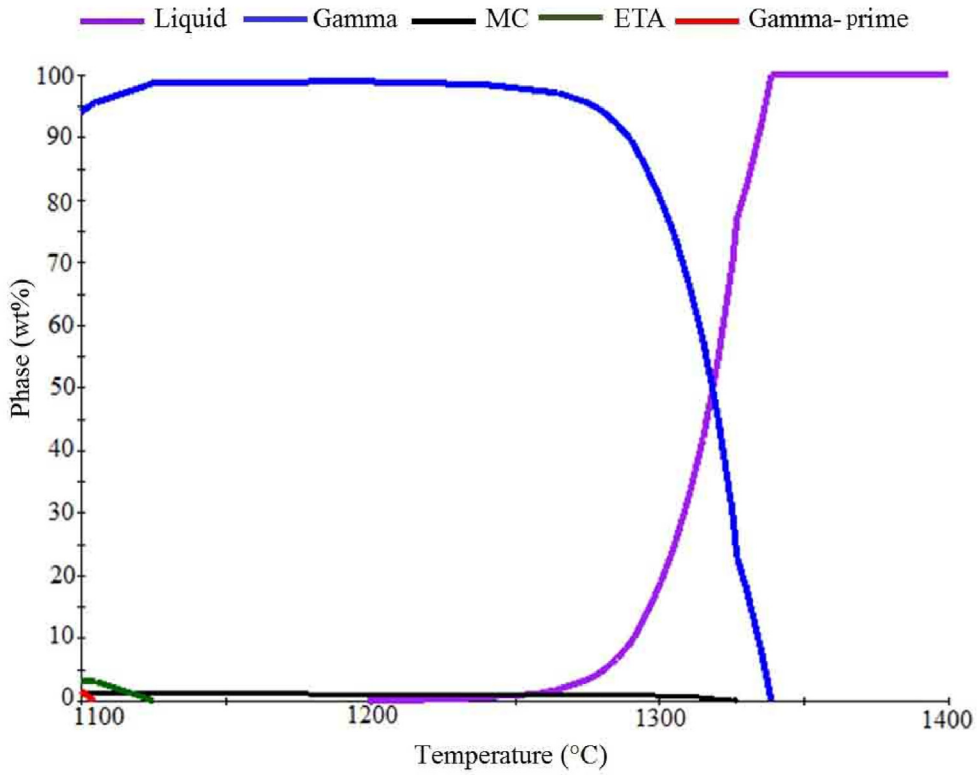

Fig. 8 – Simulation of the phase distribution in IN-939 within the solidification temperature range.

solid is anticipated to refuse the solute toward the liquid during the solidification. If $K > 1$, then the solid is supposed to absorb the solute of the liquid during the solidification.

The K values of Ni, Cr, Co and Al are greater than 1 in the solidification temperature (TS) for IN-939, as shown in Table 5, which suggests that these elements are distributed in interdendritic areas and that other elements, such as Nb, W, C, Ti and Ta, are rejected from these regions. As the temperature decreased, the MC carbides precipitated in the microstructure and the K values of Nb, W, C, Ta and Ti changed, which may lead to the formation of MC carbides, such as TiC and NBC, and γ' precipitates (Ni_3Ti) in interdendritic areas. The formation of larger precipitates along interdendritic regions is associated with the solidification process [42].

Table 5 shows the *K* values for IN-625 in the solidification temperature range. Based on the results obtained at the solidification temperature (TS), Mo obtained a *K* value greater than 1 because M_6C carbides precipitate in the microstructure. Meanwhile, the *K* values of solid solution elements, such as Ni, Cr, Mo and Co, increased due to gamma phase precipitation.

Fig. 9 shows that the gamma-prime phase, which is the most indispensable strengthening phase of BM, appears at about 1080 °C. Fig. 10 presents the analogous outcomes when the temperature varies between 800 °C and 900 °C. MC carbide entered the reaction along with the gamma matrix at this temperature range, which repels titanium and thallium. This process resulted in the germination and growth of the gamma phase and the reaction between MC carbide and the gamma phase chromium, nickel and titanium. Such reaction generates $M_{23}C_6$ carbide at temperatures above 850 °C (Equation (2)) and leads to the eta phase at temperatures below 850 °C (Equation (1)) [43].

$$K = \frac{C_s}{C_L} \tag{6}$$

3.4. *Crack measurement analysis*

Fig. 11 presents the TCL, ACL and hardness of each specimen. Results from the hardness test and metallographic studies

Table 5 – *K* values of different elements for IN-939 and IN-625.

K values of different elements											
Materials	Temperature	Nb	W	C	Ta	Ti	Mo	Al	Co	Cr	Ni
IN939	T_S = 1324 °C	0.21	0.92	0.06	0.17	0.52	0.55	1.04	1.12	1.01	1.02
	T_L = 1257 °C	6.01	1.21	248.00	4.91	6.47	0.71	0.97	1.28	1.27	0.98
IN625	T_S = 1335 °C	0.02	–	2.64	–	–	4.23	–	0.01	0.87	0.46
	T_L = 1289 °C	6.01	–	14.43	–	12.00	4.62	1.81	1.05	2.24	1.11

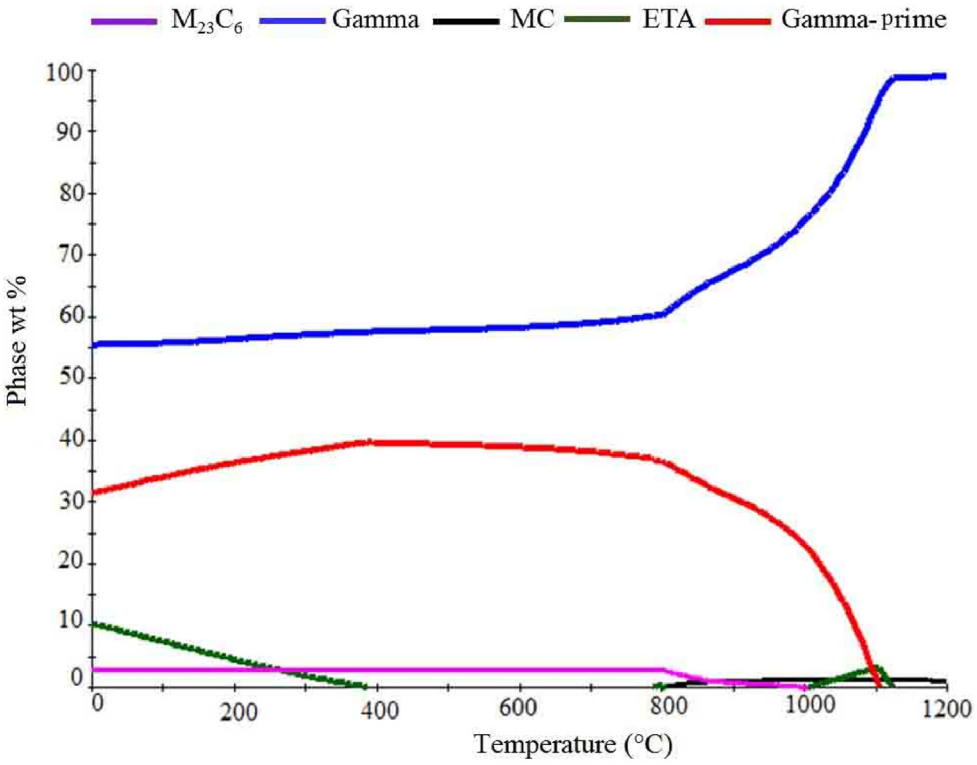

Fig. 9 – Simulation of phase distribution in IN-939.

show that the total length of welding-induced cracks considerably increases along with the hardness of HAZ [19,30,35,44]. According to previous studies, the mechanical driving force resulting from tensile welding stresses greatly influences the HAZ liquation cracking. The magnitude of welding stresses in the HAZ is significantly influenced by the ability of the alloy to relax part of the stress, which is related to the hardness of the material prior to welding. Hard base alloys with poor stress relaxation can concentrate large stresses in the relatively weakened HAZ [19,45,46]. The primary purpose of designing

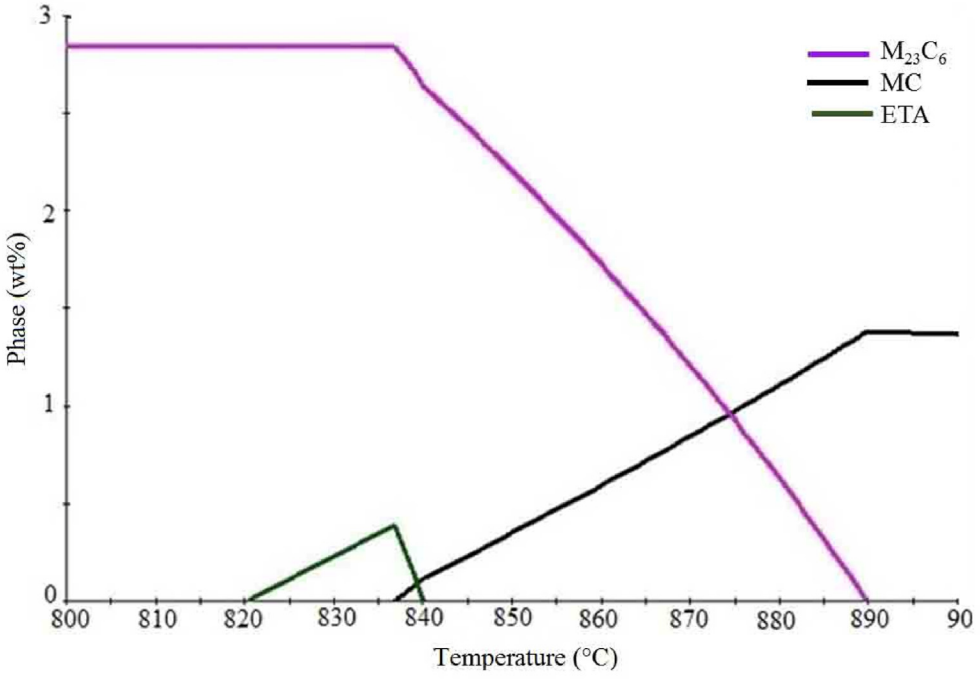

Fig. 10 – $M_{23}C_6$ carbide and eta phase precipitation at the 800 °C-900 °C temperature range.

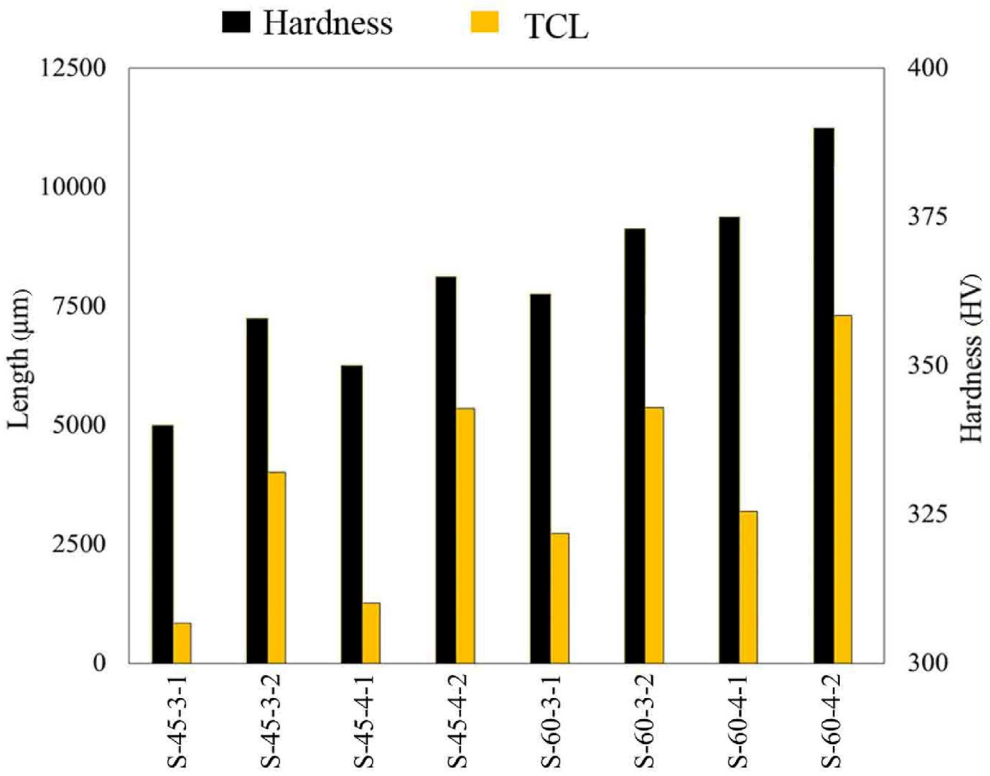

Fig. 11 – Average crack length and HAZ hardness of the samples.

experiments is to investigate the correlation between the processing factors and the data responses. In this study, the Taguchi's method, which is a powerful tool for optimizing the performance of an experimentation or production process [36], was employed to reveal the influence of the processing factors (Table 2) on TCL and ACL. Three parameters were investigated, namely layer number, pass number, and heat input at two levels. The crack measurements for different specimens are presented in Table 6 and illustrated in Fig. 11.

Given that the goal of this study was to minimize cracking, the adopted optimization logic was of minimization type (i.e., less is more). For this type of optimization, the signal-to-noise ratio (S/N) was computed as:

$$(S/N) = -10\log\left[\frac{1}{n}\sum_{j=1}^{n} Yij^2\right] \quad (7)$$

where Y_{ij} is the responses for the given factor level combination for i_{th} and j_{th} testing, 'n' is the number of responses in the factor level combination. The mean S/N ratios of control factors for each level are shown in Fig. 12.

Results of the Taguchi's optimization process are presented in Table 7. Among the three parameters, layer number has a more substantial effect on crack length than heat input and pass number. Welding in one layer and less pass with lower heat input produce cracks-free weldments.

Variance analysis (ANOVA) was applied to determine the degree of effect of the process parameters on the total crack length of each sample (Table 6). The ANOVA for the above results is shown in Tables 7 and 8, with the latter also presenting the F- and P-values for all process parameters and their interactions. The F- and P-values are significant factors that affect both TCL and ACL such that processing agents with high F-value and P-value is less than 0.05 (i.e., 95% confidence level) of the parameter. A higher F-value corresponds to a greater relative variance between groups. The P-value of the possibility is that an outcome has occurred accidently. If the P-value is less than 0.05, then the statistical test is considered

Table 6 – Specifications of the specimens and calculation of total and average crack lengths.

Experimental samples	TCL (μm)	Number of cracks	ACL (μm)
S-45-3-1	841	3	280.3
S-45-3-2	4005	11	364.1
S-45-4-1	1259	4	314.8
S-45-4-2	5347	14	381.9
S-60-3-1	2596	4	374.3
S-60-3-2	6193	18	394.1
S-60-4-1	3581	7	368.7
S-60-4-2	7202	27	397.9

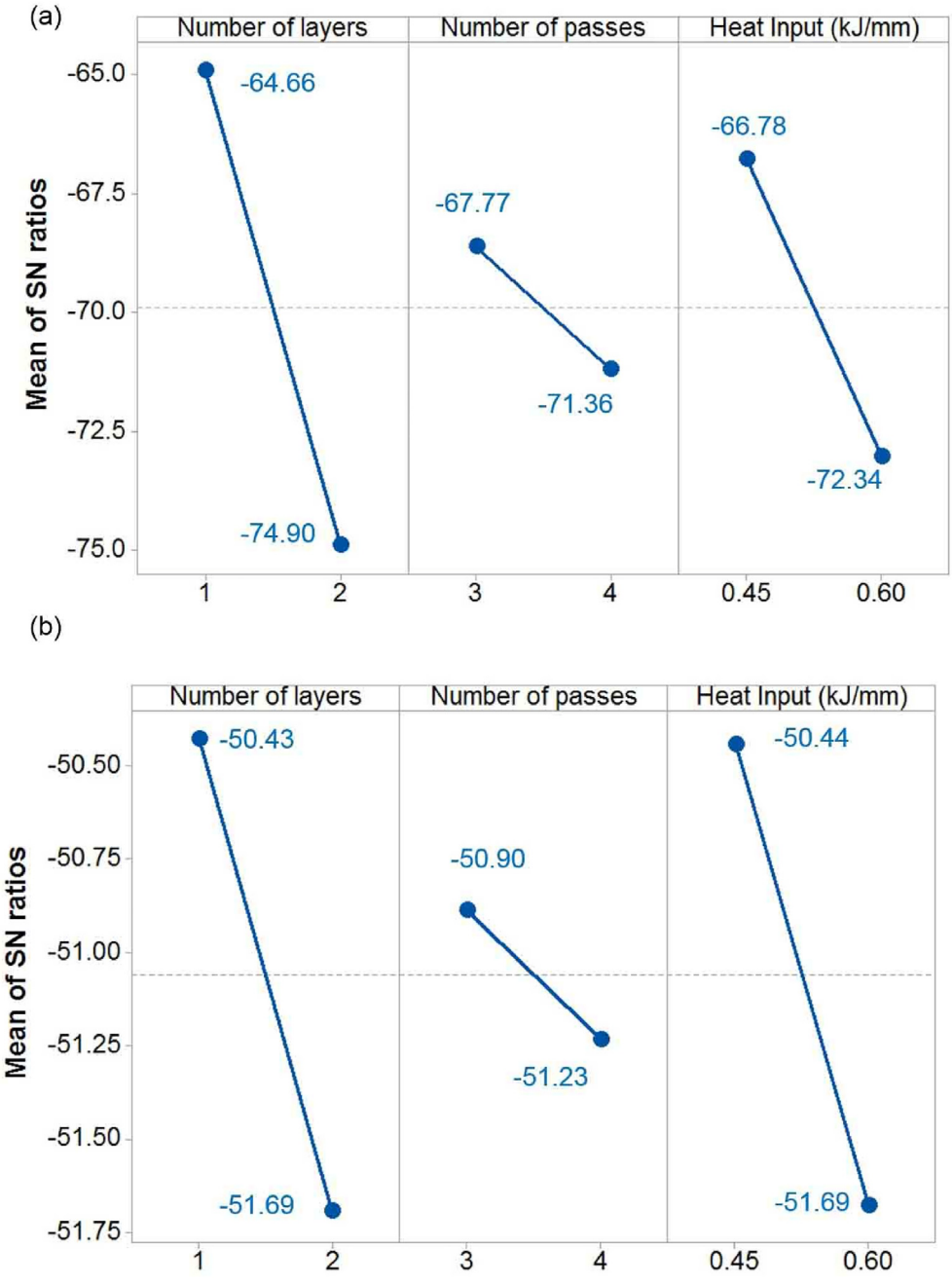

Fig. 12 – Signal-to-noise ratio at the considered levels of control factors of (a) TCL and (b) ACL.

Table 7 – Classification of the effects of research parameters.

TCL				ACL		
Level	Heat input	Pass number	Layer number	Heat input	Pass number	Layer number
1	−64.66	−67.77	−66.78	−50.43	−50.90	−50.44
2	−74.90	−71.36	−72.34	−51.69	−51.23	−51.69
Delta	5.57	3.59	13.01	1.23	0.34	1.26
Rank	2	3	1	2	3	1

Table 8 – ANOVA results for the standard deviation.

Source	DF	Contribution (%)	Adj SS	Adj MS	F-Value	P-Value
Number of layers	1	72.37	26,386,480	26,386,480	470.1	0.001
Number of passes	1	4.84	1,817,371	1,817,371	32.37	0.005
Heat input, kJ/mm	1	22.17	8,122,465	8,122,465	144.68	0.001
Error	4	00.62	224,560	224,560	–	–
Total	7	100.00	36,550,876	–	–	–

meaningful. According to Table 8, the generation of the cracks and TCL are influenced by layer number (72.37% impact percentage), followed by heat input (22.17%) and pass number (4.84%). Therefore, welding with the condition of low heat input with less number of layers and welding passes can be an effective approach to reduce liquation cracking during the repair welding of IN-939. Nevertheless, under these circumstances, liquation cracking initiates during the welding. In this regard, in order to minimize the number of cracks and achieve the optimum condition of the repair welding, a comprehensive study on the cracking phenomena and all parameters affecting the welding process is needed [47–52].

4. Conclusion

IN-939 was repaired with IN-625 via TIG welding. Given that liquid cracking is prevalent in the welding of PH-nickel superalloys, precluding IN-939 from cracking is vital. To achieve this goal, layer number, pass number and heat input were considered for repair welding. The role of these parameters in the microstructure and cracking of IN-939 was determined via comparative analysis. The following conclusions were obtained:

1) The microstructure of IN-939 was highly prone to liquation cracking. Grain boundary type cracks were formed between weld zone and HAZ interface before propagating to BM.
2) Increasing the welding heat input, pass number and layer number also increases the sensitivity of the HAZ liquation cracking. Results from the Taguchi's method and ANOVA reveal that the cracking of IN-939 during welding is influenced by layer number (72.37% impact percentage), heat input (22.17%) and pass number (4.84%). A low heat input and low layer conditions were identified as the best welding parameters that contribute to the reduction of TCL at the high-chromium Ni-based superalloy welded area.
3) The JMatPro simulation results indicate that Ni, Cr, Co and Al are distributed in interdendritic areas during welding and that other elements, such as Nb, W, C, Ti and Ta, are rejected from these areas.
4) After the welding, the hardness of IN-939 continuously decreased from 390 HV (BM) to 260 HV in the FZ (IN-625). The welding parameters and conditions significantly influenced the hardness of the HAZ, which value ranged between 330 HV and 380 HV. A close relationship was established between TCL and HAZ hardness. The total length of welding-induced cracks significantly increased along with HAZ hardness.

Declaration of Competing Interest

The authors declare that they have no known competing financial interests or personal relationships that could have appeared to influence the work reported in this paper.

REFERENCES

[1] Loto RT. Comparative study of the pitting corrosion resistance, passivation behavior and metastable pitting activity of NO7718, NO7208 and 439L super alloys in chloride/sulphate media. J Mater Res Technol 2019;8:623–9.
[2] Shang Z, Wei X, Song D, Zou J, Liang S, Liu G, et al. Microstructure and mechanical properties of a new nickel-based single crystal superalloy. J Mater Res Technol 2020;9:11641–9. https://doi.org/10.1016/j.jmrt.2020.08.032.
[3] Jin S, Li Y, Shi S, Yan Z, Chen S. Effects of Cr content on compositional evolution and precipitation kinetics of γ′ phase in Ni–Al–Cr alloy: 2D phase-field simulation. J Mater Res Technol 2020;9:7499–507.
[4] Kaplanskii YY, Zaitsev AA, Sentyurina ZA, Levashov EA, Pogozhev YS, Loginov PA, et al. The structure and properties of pre-alloyed NiAl-Cr (Co, Hf) spherical powders produced by plasma rotating electrode processing for additive manufacturing. J Mater Res Technol 2018;7:461–8.
[5] Zhuang X, Tan Y, Zhao L, You X, Li P, Cui C. Microsegregation of a new Ni-Co-based superalloy prepared through electron beam smelting and its homogenization treatment. J Mater Res Technol 2020;9(3):5422–30.
[6] Ghaderi A, Moghanni H, Dehghani K. Microstructural evolution and mechanical properties of Al0. 5CoCrFeNi high-entropy alloy after cold rolling and annealing treatments. J Mater Eng Perform 2021:1–9.
[7] Pilehrood AE, Omidvar H, Shamsipur A, Sajuri Z. Influence of transient liquid phase bonding followed by homogenization on the fatigue lifetimes of inconel 738 at elevated temperature. J Manuf Process 2020;55:348–58.
[8] Kireeva IV, Chumlyakov YI, Pobedennaya ZV, Vyrodova AV. Effect of γ′-phase particles on the orientation and temperature dependence of the mechanical behaviour of Al0.3CoCrFeNi high-entropy alloy single crystals. Mater Sci Eng A 2020;772:138772. https://doi.org/10.1016/j.msea.2019.138772.
[9] Yaer X, Shimizu K, Qu J, Wen B, Cao X, Yilagaqi, et al. Surface deformation micromechanics of erosion damage at different angles and velocities for aero-engine hot-end components. Wear 2019;426–427:527–38. https://doi.org/10.1016/j.wear.2018.12.054.
[10] Nabavi B, Goodarzi M, Khan AK. Metallurgical effects of nitrogen on the microstructure and hot corrosion behavior of Alloy 718 weldment. Mater Char 2019;157:109916. https://doi.org/10.1016/j.matchar.2019.109916.

[11] Cockings HL, Cockings BJ, Harrison W, Dowd M, Perkins KM, Whittaker MT, et al. The effect of near-surface plastic deformation on the hot corrosion and high temperature corrosion-fatigue response of a nickel-based superalloy. J Alloys Compd 2020;832:154889. https://doi.org/10.1016/j.jallcom.2020.154889.
[12] Mapelli C, Casalino C, Strada A, Gruttadauria A, Barella S, Mombelli D, et al. Comparison of the combined oxidation and sulphidation behavior of nickel- and cobalt-based alloys at high temperature. J Mater Res Technol 2020;9:15679–92. https://doi.org/10.1016/j.jmrt.2020.11.009.
[13] Shen L, Li ZR, Feng GJ, Zhang SY, Zhou Z, He P. Self-propagating synthesis joining of Cf/Al composites and TC4 alloy using AgCu filler with Ni–Al–Zr interlayer. Rare Met 2020;40:1817–24. https://doi.org/10.1007/s12598-020-01520-3.
[14] Xu S, Qi X, Xu X, Wang X, Yang Z, Zhang S, et al. Effects of electroless nickel plating method for low temperature joining ZnS ceramics. J Mater Sci Mater Electron 2019;30:15236–49. https://doi.org/10.1007/s10854-019-01896-8.
[15] Zhao W, Zhang S, Yang J, Lin T, Sekulic DP, He P. Wetting and brazing of YIG ceramics using Ag–CuO–TiO2 metal filler. J Mater Res Technol 2021;10:1158–68. https://doi.org/10.1016/j.jmrt.2020.12.080.
[16] Liu M can, min Sheng G, He H jie, Jiao Y jun. Microstructural evolution and mechanical properties of TLP bonded joints of Mar-M247 superalloys with Ni-Cr-Co-W-Ta-B interlayer. J Mater Process Technol 2017;246:245–51. https://doi.org/10.1016/j.jmatprotec.2017.03.021.
[17] Pilehrood AE, Omidvar H, Shamsipur A, Khakian-Ghomi M, Ebrahimzadeh Pilehrood A, Omidvar H, et al. Effect of transient liquid phase bonding followed by homogenization on the microstructure and hot tensile behavior of Inconel 738 superalloy. J Manuf Process 2019;48:110–8. https://doi.org/10.1016/j.jmapro.2019.10.030.
[18] Chen Z, Taheri M. The effect of pre-heating and pre-cold treatment on the formation of liquation and solidification cracks of nickel-based superalloy welded by laser beam. J Mater Res Technol 2020;9:11162–77. https://doi.org/10.1016/j.jmrt.2020.07.053.
[19] Mashhuriazar A, Omidvar H, Gur CH, Sajuri Z. Effect of welding parameters on the liquation cracking behavior of high-chromium Ni-based superalloy. J Mater Eng Perform 2020:1–10.
[20] Ola OT, Ojo OA, Chaturvedi MC. Role of filler alloy composition on laser arc hybrid weldability of nickel-base IN738 superalloy. Mater Sci Technol 2014;30:1461–9.
[21] Ye X, Hua X, Wang M, Lou S. Controlling hot cracking in Ni-based Inconel-718 superalloy cast sheets during tungsten inert gas welding. J Mater Process Technol 2015;222:381–90.
[22] Coniglio N, Cross CE. Effect of weld travel speed on solidification cracking behavior. Part 2: testing conditions and metrics. Int J Adv Manuf Technol 2020;107:5025–38. https://doi.org/10.1007/s00170-020-05232-x.
[23] Ye X, Hua X, Wang M, Lou S. Controlling hot cracking in Ni-based Inconel-718 superalloy cast sheets during tungsten inert gas welding. J Mater Process Technol 2015;222:381–90. https://doi.org/10.1016/j.jmatprotec.2015.03.031.
[24] Kazempour-Liasi H, Tajally M, Abdollah-Pour H. Liquation cracking in the heat-affected zone of IN939 superalloy tungsten inert gas weldments. Int J Miner Metall Mater 2020;27:764–73. https://doi.org/10.1007/s12613-019-1954-y.
[25] Guzman I, Saucedo E, Gonza MA, Gonza MA. Effect of preweld heat treatment on the microstructure of heat-affected zone (HAZ) and weldability of Inconel, vol. 23; 2014. p. 1125–30. https://doi.org/10.1007/s11665-013-0704-y.
[26] González MA, Martínez DI, Pérez A, Guajardo H, Garza A. Microstructural response to heat affected zone cracking of prewelding heat-treated Inconel 939 superalloy. Mater Char 2011;62:1116–23. https://doi.org/10.1016/j.matchar.2011.09.006.
[27] Kazempour-Liasi H, Tajally M, Abdollah-Pour H. Effects of pre- and post-weld heat treatment cycles on the liquation and strain-age cracking of IN939 superalloy. Eng Res Express 2019;1. https://doi.org/10.1088/2631-8695/ab4d6c.
[28] Chen Y, Zhang K, Huang J, Hosseini SRE, Li Z. Characterization of heat affected zone liquation cracking in laser additive manufacturing of Inconel 718. Mater Des 2016;90:586–94. https://doi.org/10.1016/j.matdes.2015.10.155.
[29] Álvarez Tejedor, Singh, Pilidis. 13 - Maintenance and repair of gas turbine components. Modern Gas Turbine Systems. Woodhead Publishing; 2013. p. 565–634. 978-1-84569-728-0, https://www.sciencedirect.com/science/article/pii/B9781845697280500136.
[30] Mashhuriazar A, Omidvar H, Sajuri Z, Gur CH, Baghdadi AH. Effects of pre-weld heat treatment and heat input on metallurgical and mechanical behaviour in HAZ of multi-pass welded IN-939 superalloy. Metals (Basel) 2020;10:1453.
[31] Tajally M. Effects of filler metals on heat-affected zone cracking in IN-939 superalloy gas-tungsten-arc welds. J Mater Eng Perform 2020;738. https://doi.org/10.1007/s11665-020-04617-z.
[32] Abedini M, Jahangiri MR, Karimi P. Rejuvenation of the microstructure and mechanical properties of a service-exposed IN939 superalloy by heat treatments. Mater A T High Temp 2019;36:19–26.
[33] Lvov G, Levit VI, Kaufman MJ. Mechanism of primary MC carbide decomposition in Ni-base superalloys. Metall Mater Trans A 2004;35:1669–79.
[34] Hu R, Bai G, Li J, Zhang J, Zhang T, Fu H. Precipitation behavior of grain boundary M23C6 and its effect on tensile properties of Ni–Cr–W based superalloy. Mater Sci Eng A 2012;548:83–8.
[35] Kazempour-Liasi H, Tajally M, Abdollah-Pour H. Effects of pre-and post-weld heat treatment cycles on the liquation and strain-age cracking of IN939 superalloy. Eng Res Express 2019;1:25026.
[36] Li S, Li K, Cai Z, Pan J. Behavior of M23C6 phase in Inconel 617B superalloy during welding. J Mater Process Technol 2018;258:38–46.
[37] Yan F, Liu S, Hu C, Wang C, Hu X. Liquation cracking behavior and control in the heat affected zone of GH909 alloy during Nd: YAG laser welding. J Mater Process Technol 2017;244:44–50.
[38] Donachie MJ, Donachie SJ. SUPERALLOYS Second Edition. 2002. https://doi.org/10.1089/jwh.1.1999.8.637.
[39] Zhang Z, Huang X, Yao P, Xue J. A new method for weld dilution calculation through chemical composition analysis. Metals (Basel) 2021;11:1–10. https://doi.org/10.3390/met11010131.
[40] Yu K, Jiang Z, Li C, Chen S, Tao W, Zhou X, et al. Microstructure and mechanical properties of fiber laser welded GH3535 superalloy. J Mater Sci Technol 2017;33:1289–99. https://doi.org/10.1016/j.jmst.2016.11.026.
[41] Lippold JC, Kiser SD, DuPont JN. Welding metallurgy and weldability of nickel-base alloys. John Wiley & Sons; 2011.
[42] Marchese G, Parizia S, Saboori A, Manfredi D, Lombardi M, Fino P, et al. The influence of the process parameters on the densification and microstructure development of laser powder bed fused inconel 939. Metals (Basel) 2020;10:1–19. https://doi.org/10.3390/met10070882.
[43] Cueto-Rodriguez MM, Avila-Davila EO, Lopez-Hirata VM, Saucedo-Muñoz ML, Palacios-Pineda LM, Trapaga-Martinez LG, et al. Numerical and experimental analyses of the effect of heat treatments on the phase stability of inconel 792. Ann Mater Sci Eng 2018;2018.

[44] Kazempour-Liasi H, Tajally M, Abdollah-Pour H. Liquation cracking in the heat-affected zone of IN939 superalloy tungsten inert gas weldments. Int J Miner Metall Mater 2020;27:764–73.
[45] Egbewande AT, Buckson RA, Ojo OA. Analysis of laser beam weldability of Inconel 738 superalloy. Mater Char 2010;61:569–74.
[46] Egbewande AT, Zhang HR, Sidhu RK, Ojo OA. Improvement in laser weldability of INCONEL 738 superalloy through microstructural modification. Metall Mater Trans A 2009;40:2694.
[47] Akbarpour MR, Mashhuriazar A, Daryani M. Experimental and numerical investigation on the effect of the tempcore process parameters on microstructural evolution and mechanical properties of dual-phase steel reinforcing rebars. Met Mater Int 2020:1–10.
[48] Ahmadi MH, Ahmadi MA, Pourfayaz F. Performance assessment and optimization of an irreversible nano-scale Stirling engine cycle operating with Maxwell-Boltzmann gas. Eur Phys J Plus 2015;130. https://doi.org/10.1140/epjp/i2015-15190-5.
[49] Samiun WS, Ashari SE, Salim N, Ahmad S. Optimization of processing parameters of nanoemulsion containing aripiprazole using response surface methodology. Int J Nanomed 2020;15:1585–94. https://doi.org/10.2147/IJN.S198914.
[50] Do-sik S. Effects of process parameters on additive manufacturing of aluminum porous materials and their optimization using response surface method. J Mater Res Technol 2021. https://doi.org/10.1016/j.jmrt.2021.08.010.
[51] Medeiros GB, de Souza PR, Retamiro KM, Nakamura CV, Muniz EC, Corradini E. Experimental design to evaluate properties of electrospun fibers of zein/poly (ethylene oxide) for biomaterial applications. J Appl Polym Sci 2021:50898.
[52] Attarilar S, Gode C, Mashhuriazar MH, Ebrahimi M. Tailoring twist extrusion process; the better strain behavior at the lower required loads. J Alloys Compd 2020:157855.